



Multi-physics rock templates to seismically characterise complex carbonates

Alireza Shahin^a, Mike Myers^b and Lori Hathon^b

^aDepartment of Geology, University of Isfahan, Isfahan, Iran; ^bPetroleum Department, Cullen College of Engineering, University of Houston, Houston, TX, USA

ABSTRACT

Single-physics rock templates have been widely addressed in the literature especially for sandstone reservoirs. Nevertheless, multi-physics rock templates (MPRT) have not been broadly studied to characterise complex carbonates. Multi-physics measurements lead to generate MPRTs which provide visual aid to petrophysicists and seismic rock physicists to classify facies and determine reservoir rock and fluids. Our research is oriented around two sequential stages. In the first stage, we make three independent porosity measurements (Archimedes, μ CT and NMR) on core carbonate plugs from northern Niagaran reef. Resistivity, P&S-wave ultrasonic measurement and joint modelling of the same brine saturated plugs help us to fine-tune the model parameters through a global optimisation algorithm. Optimisation algorithm provides vuggy and micro-porosities close to independently measured porosities using NMR and μ CT. In the second stage, we extend the technique from core data to well logs. We integrate mass balance equations to model bulk density and staged differential effective medium (SDEM) theory to model elastic and electrical resistivity of dual-porosity carbonates. Then, we design a stochastic global algorithm to simultaneously invert petrophysical properties. The inversion algorithm iteratively recovers the petrophysical properties including intergranular porosity, vuggy porosity, water saturation, salinity and matrix properties. Critical porosity, resistivity lithology exponents and sonic length scales for different pore systems are also estimated with meaningful accuracy.

ARTICLE HISTORY

Received 20 October 2020
Accepted 16 November 2021

KEY WORDS

Carbonate; rock physics;
seismic reflection; modelling

Introduction

Statistical rock physics combined with cross-plotting techniques have been performed to map probabilistic litho-fluid facies (Avseth et al. 2001; Mukerji et al. 2001). The most popular cross-plotting technique is called the rock physics template (RPT). In RPT analysis, the depositional and diagenetic trend models are combined with Gassmann fluid substitution to make cross-plots of elastic parameters, e.g. Poisson ratio versus acoustic impedance. Using the RPTs, one can distinguish the litho-fluid effects and to extract some of the petrophysical properties from inverted elastic parameters (Avseth, Mukerji, and Mavko 2005).

A major portion of the world's oil and gas reserves are in carbonate reservoirs. However, the development of forward models for predicting the physical properties of carbonate rocks has not been as successful as similar efforts for clastic reservoirs. This is a result of the large influence of diagenesis which often plays the primary role in defining the character of carbonate rock.

Kazatchenko, Markov, and Mousatov (2003) proposed a technique for quantitative estimation of secondary porosity (e.g. cracks or vugs) using sonic and ultrasonic well log and core measurements. In their model, a double-porosity rock consists of grains, primary porosity and secondary porosity. Effective

medium approximation (EMA) was applied to calculate P&S-wave velocities. Spheroids with different aspect ratios, i.e. inclusion, were utilised to model all the rock components. Matrix P&S-wave velocities were first calculated as functions of the primary porosity. Elastic moduli of the skeleton were computed using the volume concentration of minerals or defined by laboratory data. They determined aspect ratios for grains and primary pores by the inversion of published P&S-wave velocities. Then, the aspect ratio of secondary pores was estimated by minimising the difference between simulated velocities and the measured P&S-velocities using joint inversion. The type of secondary-pore system (cracks or vugs) is indicated by the obtained aspect ratio of inclusions.

Rovetta, Colombo, and Turkoglu (2017) developed a petrophysical joint inversion (PJI) algorithm and tested it on a carbonate reservoir in Saudi Arabia. They utilised Archie (Archie 1962) and Gassmann (Gassmann 1951) models to simulate electrical resistivity and sonic well logs. Porosity and fluid saturation were the petrophysical properties retrieved in PJI by inverting density, resistivity and sonic well logs. They showed that the PJI resulted in porosity which was in good agreement with independently measured neutron porosity.

Salma, Turkoglu, and Rovetta (2018) applied the same PJI as Rovetta, Colombo, and Turkoglu (2017) on a carbonate reservoir in Saudi Arabia. In their Bayesian inversion approach, prior knowledge of both solid matrix and fluid properties was the key factors to reduce ambiguity. Total dissolved solids (TDS) measured in the lab showed high variability amongst the wells. Because water salinity changed water resistivity, any change in salinity impacted the estimated hydrocarbon saturation. To enhance the performance of PJI in predicting porosity and saturation, they utilised an offline statistical workflow to estimate water resistivity.

In this research paper, we first develop multi-physics rock templates (MPRT) on core scale measurements. Next, we construct resistivity, elastic and density borehole-derived well logs for complex carbonates and demonstrate the value of MPRT using an inversion workflow which jointly converts well logs into petrophysical properties. For doing so, we utilise a global optimisation machine called Very Fast Simulated Annealing (VFSA) similar to Shahin, Myers, and Hathon 2020. Primary porosity, secondary porosity, water saturation, matrix density, matrix bulk & shear moduli, salinity, critical porosity, resistivity lithology exponents, and elastic length scales are petrophysical, matrix, fluid and model parameters recovered.

Pore combination modelling to simulate electrical resistivity

Electrical-resistivity (inverse of conductivity) has been widely utilised to evaluate the hydrocarbon content of petroleum reservoirs. At the heart of formation evaluation, there exists "Archie's equation" (Archie 1962) to compute water saturation knowing reservoir porosity, brine resistivity, lithology or cementation exponent (m), and saturation exponent (n).

While Archie's model is mainly valid for single pore and clay-free formations, other models have been proposed for complex rocks with multiple pore structure. Pore combination modelling (PCM) methodology (Myers 1989, 1991) is one of those models which expresses the contribution of each pore structure and its fluid content in permeability and resistivity. PCM is an extension of Archie's model representing rocks with multiple pore structures. Thanks to universal carbonate core measurements, Myers (1991) obtained Archie's lithology exponents for vuggy, intergranular and microporosity pore types of carbonate formations worldwide. As summarised by Shahin, Myers, and Hathon (2020), the following equation gives the formation factor of a water-bearing rock with two pore structures:

$$F = \left(\frac{1}{\phi_i} \right)^{\lambda_i} \left(\frac{\phi_i}{\phi_i + \phi_v} \right)^{\lambda_v} \quad (1)$$

F is the ratio of the resistivity of 100% water-saturated rock to brine resistivity called formation factor. ϕ_i and ϕ_v are the fractional primary (intergranular or micro) and secondary (vugs and cracks) porosities, respectively. $\phi_t = \phi_i + \phi_v$ is the total porosity. λ_i is the lithology exponent for primary pores and λ_v is the lithology exponent for secondary pores. In the following, we will present new methodologies to obtain the primary and secondary lithology exponents using resistivity core measurements and well logs via global optimisation. Figure 1 represents the PCM methodology for a dual pore carbonate formation. In this figure, the formation factor (F) versus total porosity, i.e. $F - \phi_t$ are plotted in log-log plane. Starting from point ($F = 1$ and $\phi_t = 1$) a blue line with slope of λ_i illustrates the gradual decrease in total porosity due to sediment compaction. At this stage, primary pores are the only pore system and total porosity (ϕ_t) is equal to primary porosity of ϕ_i . Then, diagenesis comes into play and secondary pores start to evolve. A black line with slope of λ_v represents the evolving of the secondary porosity of ϕ_v . This line has a different slope than the line of primary pores. When the diagenesis process is finished, the sample has a total porosity of ϕ_t which is the summation of ϕ_v and ϕ_i . The red line connecting the final position of the sample in $F - \phi_t$ plane with the point of ($F = 1$, $\phi_t = 1$) is the Archie's line with slope of (m) representing the lithology exponent.

Staged differential effective medium to model elastic moduli

Reuss lower bound and Voight upper bound have been historically utilised to associate the elastic moduli of rock components with the elastic moduli of the mixture. While the moduli of the mixtures are always located between these bounds (Mavko, Mukerji, and Dvorkin 2020), several researchers attempted to better locate moduli exact position by adding more textural information on how grains and pores are structured within the rocks. One of such attempts was the work by Myers and Hathon (2012) who extended the differential effective medium theory by introducing the concept of "Staging" on how the process of sedimentation, lithification/ compaction, and diagenesis lead to form sedimentary rocks. In the staged differential effective medium (SDEM) technique, inclusions of different length scale (aspect ratio) are gradually added to a host assuming they only feel the average properties of the host and neglecting interaction terms between the inclusions.

Similar to PCM to model resistivity, SDEM methodology models the elastic moduli of dual-porosity carbonates. PCM is a special case of SDEM, and these are general techniques for modelling the impact of mineralogy and texture on permeability, resistivity and elastic measurements.

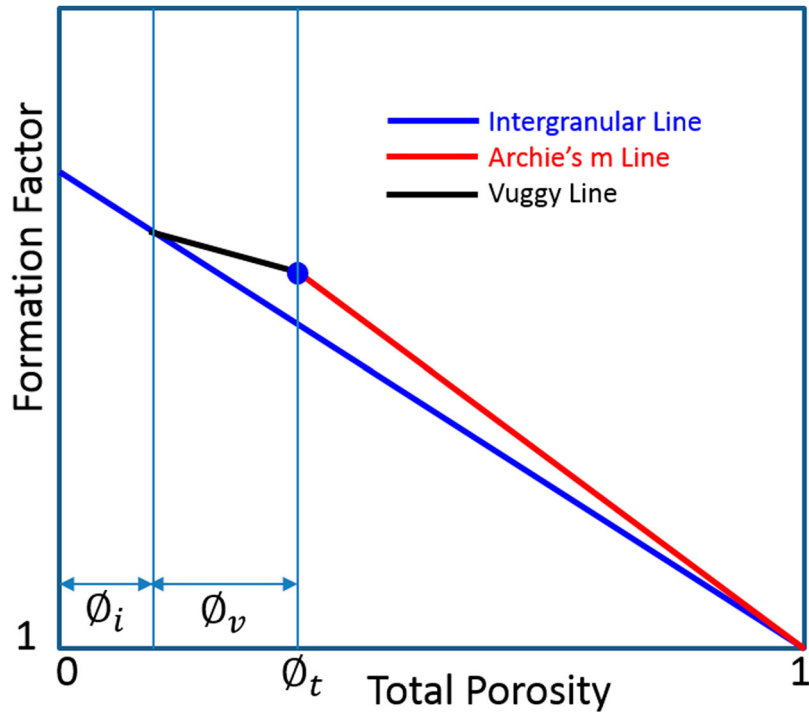


Figure 1. A graphical representation of pore combination modelling (PCM).

The well-known critical porosity (Nur et al. 1995) model is inherently included in SDEM (Myers and Hathon 2012). To simulate the elastic moduli of a single-pore carbonate, we need a two-staged SDEM. The first step is to integrate the elastic moduli from the host to the critical porosity with a length scale of $L = 0$ which mimics an iso-stress Reuss bound. The second step is to integrate from critical porosity to total porosity with a length scale of $L \neq 0$ using

$$M = M_c \frac{1 + \left(\frac{\phi_c - \phi}{\phi_c}\right) \cdot \left(\frac{M_i - M_c}{M_c}\right) \cdot L}{1 - \left(\frac{\phi_c - \phi}{\phi_c}\right) \cdot \left(\frac{M_i - M_c}{M_i}\right) \cdot (1 - L)} \quad (2)$$

where ϕ_c is the critical porosity, M_i is the inclusions' modulus, L is the length scale and related to this inclusion. The modulus M_c can be calculated using the iso-stress bound (Reuss lower bound) for the mixture of the host and grain at the critical porosity.

A dual-porosity carbonate can be simulated by adding integration step to model the secondary porosity (Myers and Hathon 2012). Figure 2 illustrates the SDEM technique for a dual-porosity formation. The elastic moduli (bulk and shear) are plotted versus total porosity (ϕ_t). The bound corresponding to the length scale of L_i connects the elastic moduli at critical porosity (M_c) to elastic moduli at zero porosity (Solid or matrix moduli). This bound is associated with primary pores. The bound corresponding to the length scale of L_v which does not pass through elastic moduli at critical porosity is associated with the moduli change due

to change in secondary porosity. For a formation consisting of primary and secondary pores, the secondary-porosity bound intersects the primary bound at the primary porosity. In this plot, ϕ_i is the primary porosity, ϕ_v is the secondary porosity and the sum $\phi_t = \phi_i + \phi_v$ is the total porosity. Starting from point (ϕ_c, M_c) the blue bound with length scale of L_i illustrates the gradual decrease in total porosity due to sediment compaction. At this stage, primary pores are the only pore system and total porosity (ϕ_t) is equal to primary porosity of ϕ_i . Then, diagenesis comes into play and vugs start to evolve. A black bound with length scale of L_v represents the evolving of the secondary porosity of ϕ_v . This bound has a different length scale than the bound of primary pores. When the diagenesis process is finished, the sample has a total porosity of ϕ_t which is the summation of ϕ_v and ϕ_t . The red bound connecting the final position of sample in $M - \phi_t$ plane with the point of (ϕ_c, M_c) is the Semi-Archie's line described in Figure 1.

In the following, we will present new methodologies to obtain matrix elastic moduli, critical porosity, primary and secondary's L parameters, and lithology exponents of each pore system from sonic and resistivity core measurements and well logs via global optimisation.

Mass conservation to replicate bulk density

The following mass balance equations are used to replicate bulk density for core and well log measurements. For this particular exercise, we use tabulated calcite density of 2.71 g/cm^3 , brine with density of 1.05 g/cm^3

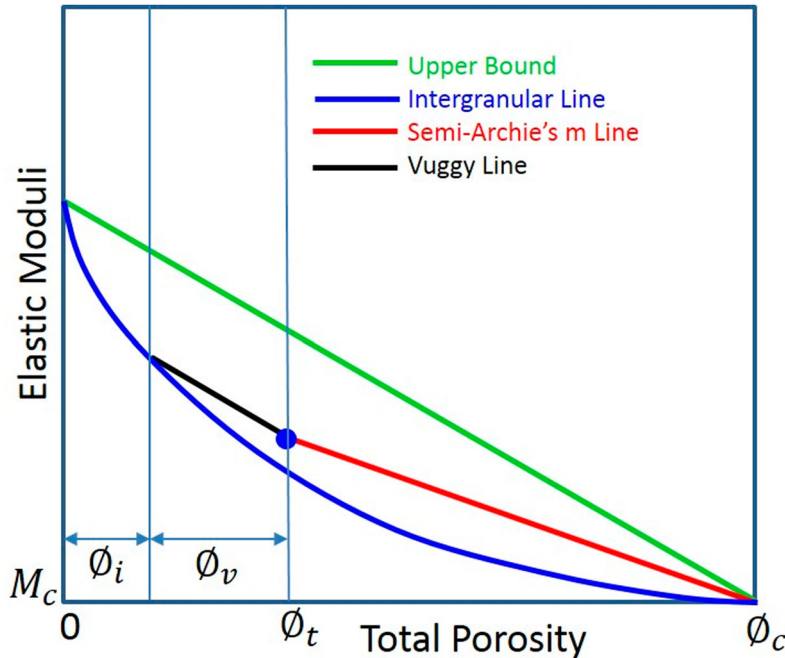


Figure 2. Illustration of staged differential effective medium (SDEM) technique for a dual-porosity carbonate.

and oil with density of 0.75 g/cm³. In Equations (3) and (4), ρ_b , ρ_{ma} , ρ_f , ρ_o and ρ_w are bulk density, matrix density, fluid density, oil density and brine density, respectively. ϕ_t is the total porosity of $\phi_t = \phi_i + \phi_v$, and S_{wt} is the total water saturation occupying primary and secondary pores.

$$\rho_b = \rho_{ma}(1 - \phi_t) + \rho_f\phi_t \quad (3)$$

$$\rho_f = \rho_o(1 - S_{wt}) + \rho_w S_{wt} \quad (4)$$

Multi-physics rock templates of carbonates on core scale

We have used 11 core plugs in this study. They are dolomite samples from the Pinnacle Reef Trend, Michigan. They were measured under ambient conditions (Table 1). Three independent porosity measurements on carbonate core plugs have been made. These include porosities obtained from Archimedes, micro-computerised tomography (μ CT) and nuclear magnetic resonance (NMR). In Archimedes technique, the weight of core plugs in dry, saturated and submerged conditions, pore volumes and porosity are determined. This technique is still the most accurate method to estimate total porosity. The porosity of core plugs using this method varies between 5 and 16 porosity units.

In μ CT technique, X-rays are utilised to provide high-resolution images of geometry and microstructures. In Figure 3, vertical and horizontal slices of the 3D volume are displayed. A significant portion of the pore type are vugs and no other visible pore type can be seen using μ CT. We performed a segmentation technique using colour classification to measure the vuggy porosity of the core plugs. On average, μ CT-derived porosities are smaller than those estimated from Archimedes and

Table 1. The specifications of the core samples.

Sample no.	Lithology	Diameter (cm)	Length (cm)	Lab. condition
A1	Dolomite	2.55	5.08	Ambient
A2	Dolomite	2.54	5.07	Ambient
A3	Dolomite	2.54	5.07	Ambient
A4	Dolomite	2.54	5.06	Ambient
B1	Dolomite	2.54	5.05	Ambient
B2	Dolomite	2.54	5.06	Ambient
B3	Dolomite	2.55	5.08	Ambient
B4	Dolomite	2.53	5.08	Ambient
B5	Dolomite	2.53	5.01	Ambient
B6	Dolomite	2.53	5.03	Ambient
B7	Dolomite	2.54	5.04	Ambient

NMR. This is consistent with the fact that μ CT cannot resolve the microporosity.

The NMR measurements for porosity closely follow Archimedes porosities within 1–2 porosity units. The smaller value for the NMR may be due to extremely small pores beyond the resolution of the NMR. Figure 4 shows the distributions of samples used in this research. To better predict the contribution of each pore type, we choose to fit a Weibull distribution to NMR response. To estimate the model parameters for curve-fitting exercise a stochastic global optimisation technique called very fast simulated annealing (VFSA) has been utilised. Several authors find VFSA (Ingber 1989, 1993), as an amazing optimiser which not only is a global search engine but also a stochastic one. Monte Carlo Guided (MCG) search is at the heart of VFSA. Samples in model space are taken using MCG from 1D Cauchy distribution which is a function of so call temperature.

The probability density function (PDF) for Weibull distribution is given as

$$f(x; \lambda, k) = \frac{k}{\lambda} \left(\frac{x}{\lambda}\right)^{k-1} \exp\left[-\left(\frac{x}{\lambda}\right)^k\right] x \geq 0$$

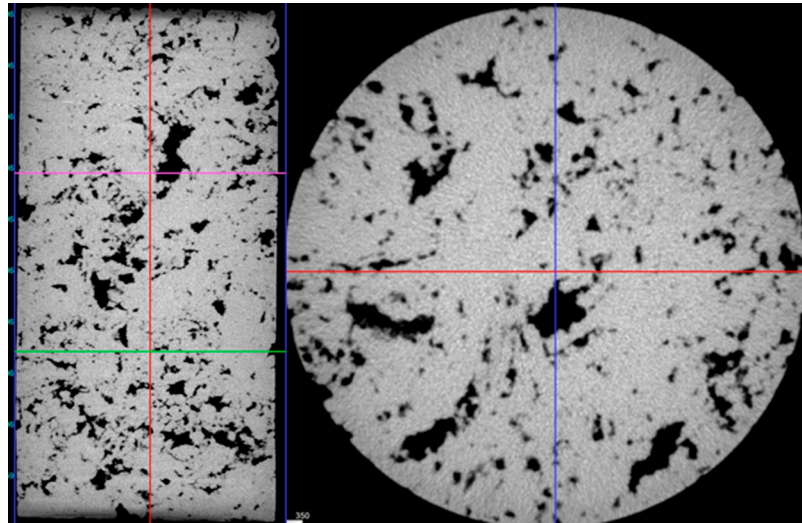


Figure 3. Micro-CT scan of the carbonate core plug. The left image is horizontal and the right one is a vertical slice through the 3D image acquired. Note that the majority of the pore volume is vugs and microporosity is not visible.

$$k > 0 \text{ shape factor } \lambda > 0 \text{ scale factor} \quad (5)$$

where x is the independent variable; and k and λ are the fitting (model) parameters in Weibull distribution and referred to shape factor and scale factor, respectively. Most of the NMR distributions of our samples display bimodal behaviour, so we add up two Weibull distributions with different weighting factors α as

$$\begin{aligned} f(x; \lambda_1, k_1, \lambda_2, k_2, \alpha_1, \alpha_2) \\ = \alpha_1 f_1(x; \lambda_1, k_1) + \alpha_2 f_2(x; \lambda_2, k_2) \end{aligned} \quad (6)$$

where $\alpha_1 + \alpha_2 = 1$

where α_1 and α_2 are the weighting factors for each Weibull distribution. Similar to Equation (5), k and λ are shape and scale factors, respectively, for each Weibull distribution.

The normalised error or objective function for the VFSA optimisation is as follows:

$$E(x; \lambda_1, k_1, \lambda_2, k_2, \alpha_1, \alpha_2) = \frac{2 \sum_{i=1}^n [f(x_i) - \text{NMR } T_2(i)]}{\sum_{i=1}^n [f(x_i) + \text{NMR } T_2(i)]} \quad (7)$$

NMR T_2 data are discretised in T_2 domain with n the number of total samples and x is

$$x = \ln \frac{T_2}{T_{2,0}} \quad (8)$$

$T_{2,0}$ is the smallest T_2 used in the T_2 distribution (here 0.01 ms). There are five independent model parameters, i.e. $\lambda_1, k_1, \lambda_2, k_2, \alpha_1$, to fit for each core plug. It is worth noting that the extension of this approach to tri-modal distribution is straightforward where there will be eight model parameters to fit the NMT T_2 distribution. The fitting can be formulated as a constrained non-linear optimisation which we addressed via VFSA in this paper.

The optimised model parameters have been used in decomposing the NMR T_2 response of all core plugs and then vuggy and microporosity of each core plug computed. Figure 4 illustrates the NMR T_2 distribution and the associated bimodal Weibull distribution fits for one of the core plugs.

Analysing the NMR response of all core plugs, we conclude that on average vugs contribute 80–95 percent of NMR total porosity and only a small fraction associated with microporosity. The NMR measurements provide convincing evidence that a dual pore system exists in these core plugs consisting of a connected microporosity with vugs. This information is vital for the SDEM resistivity and velocity modelling in the next part.

The formation factor versus total Archimedes porosity is plotted in Figure 5. The different blue lines all extrapolated to $F = 1$ and $\phi_t = 1$ are for λ_m from 0 to 3. One of these lines (red one) is the microporosity line best explained the petrophysical characteristics of these core plugs. There is a large scatter of these data points (displayed in rhombus) about any of the lines because there are two pore types present and the amounts of both are changing. Figure 6 displays the same data plotted in $F - \phi$ log-log plane. The microporosity trend line selected for the data set is obtained from the non-linear optimisation. The position that vuggy porosity lines intersect the microporosity line will provide the amount of each individual porosity. The vuggy porosity computed from resistivity modelling along with the vuggy porosity derived from velocity modelling will be used later in an inversion machine to optimise model parameters of both velocity and resistivity models.

Figure 7 illustrates the Reuss and Voight average bounds for the carbonate core plugs. Different values of L for both bulk and shear moduli are also depicted. One of these lines (black one) is the microporosity line

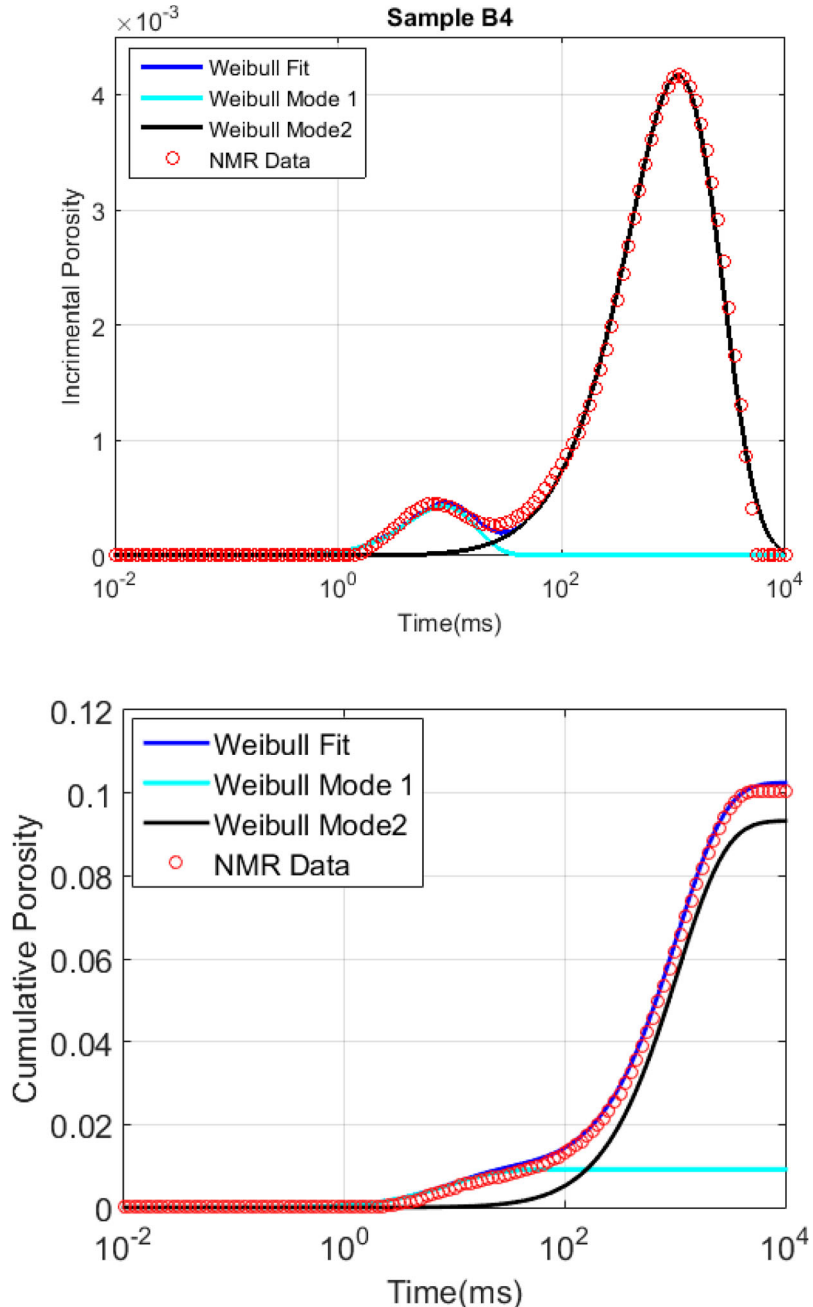


Figure 4. Top panel shows NMR T_2 distribution and the associated bimodal Weibull distribution fit. The dots are NMR measurements (10 porosity unit). The solid black line is Weibull fit to the second mode or pore type which are vugs (9 porosity unit). The cyan solid line is the Weibull distribution of the first mode or pore type which is microporosity (less than 1 porosity unit). The bottom panel shows the cumulative distribution of NMR T_2 signal displayed in the top panel.

best explained the moduli of these core plugs. Similar to the resistivity model there is no obvious trend in these data because there are two pore types present and the amounts of both are changing. Figure 8 displays the same data as shown in Figure 7. The microporosity and vuggy porosity trends selected for the data set are obtained from the non-linear optimisation of velocity and resistivity data. The position that vuggy porosity lines intersect the microporosity line provides the amount of each individual porosity. The vuggy porosity computed from velocity modelling along with the vuggy porosity derived from resistivity modelling will be used later in an inversion machine to optimise the

model parameters of both velocity and resistivity models.

To optimise the SDEM model parameters, we define an objective function as the difference between vuggy porosities predicted from resistivity modelling (ϕ_i^{vr}) and the vuggy porosities computed from velocity modelling (ϕ_i^{vk}, ϕ_i^{vs} for bulk and shear moduli, respectively) to be minimised. Index i indicates core plug numbers from 1 to n .

$$\begin{aligned} E(\phi_c, M_k, M_s, \lambda_m, \lambda_v, L_{ms}, L_{mk}) \\ = \frac{2 \sum_{i=1}^n [\phi_i^{vk} - \phi_i^{vs}]}{\sum_{i=1}^n [\phi_i^{vk} + \phi_i^{vs}]} \end{aligned}$$

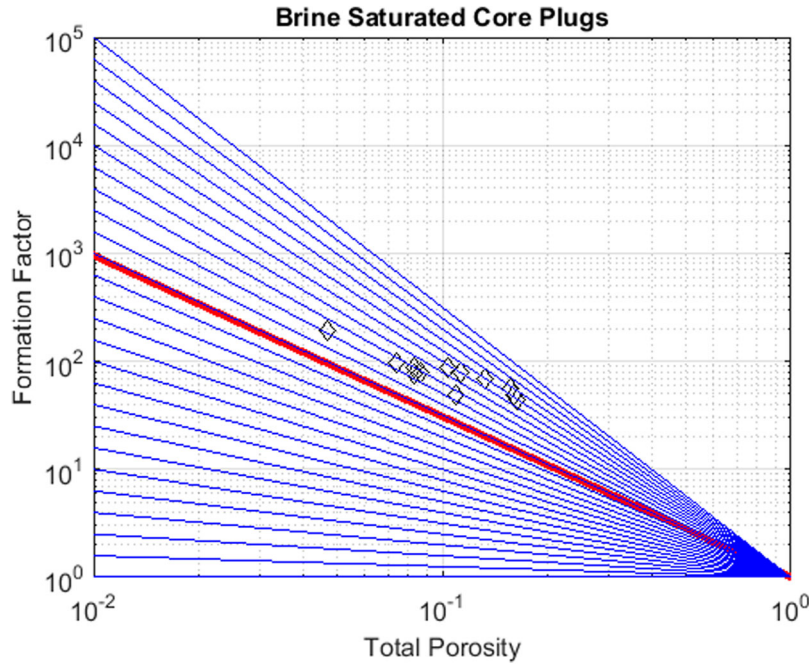


Figure 5. The plot of the formation factor versus Archimedes porosity. No trend exists because there is a dual pore system of micro-pores and vugs. Rhombus is the core plug measurements.

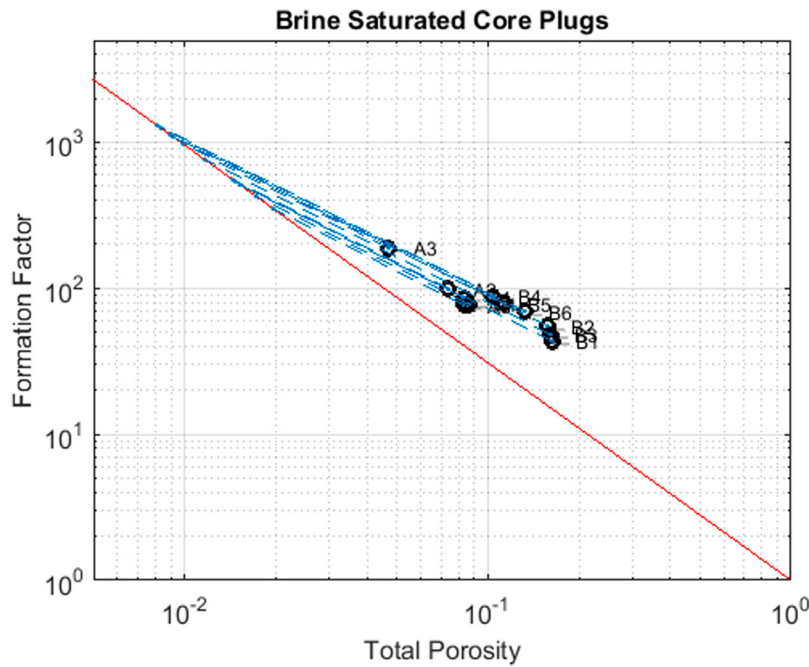


Figure 6. The plot of the formation factor versus Archimedes porosity. The optimum microporosity lithology exponent (red line) is obtained from non-linear optimisation. The dashed blue lines are the optimum lithology exponent for vugs. Circles are the core plug measurements.

$$+ \frac{2 \sum_{i=1}^n [\phi_i^{vk} - \phi_i^{vr}]}{\sum_{i=1}^n [\phi_i^{vk} + \phi_i^{vr}]} \quad (9)$$

SDEM model parameters are critical porosity (ϕ_c), bulk (M_k) and shear (M_s) moduli of grains, microporosity lithology exponent for resistivity (λ_m), vuggy porosity lithology exponent for resistivity (λ_v), microporosity parameter for shear modulus (L_{ms}), microporosity parameter for bulk modulus (L_{mk}). Vuggy porosity L

parameters for bulk and shear moduli are set to 1.0 based on the previously published results (Myers and Hathorn 2012). Table 2 summarises all the model parameters as well as their mean values for 200 runs of VFSA each with 200 iterations. Figure 9 displays the correlation of vuggy porosity estimated from velocity and resistivity. It also shows a high correlation between vuggy porosity jointly estimated from velocity-resistivity and the ones estimated from NMR and μ CT measurements.

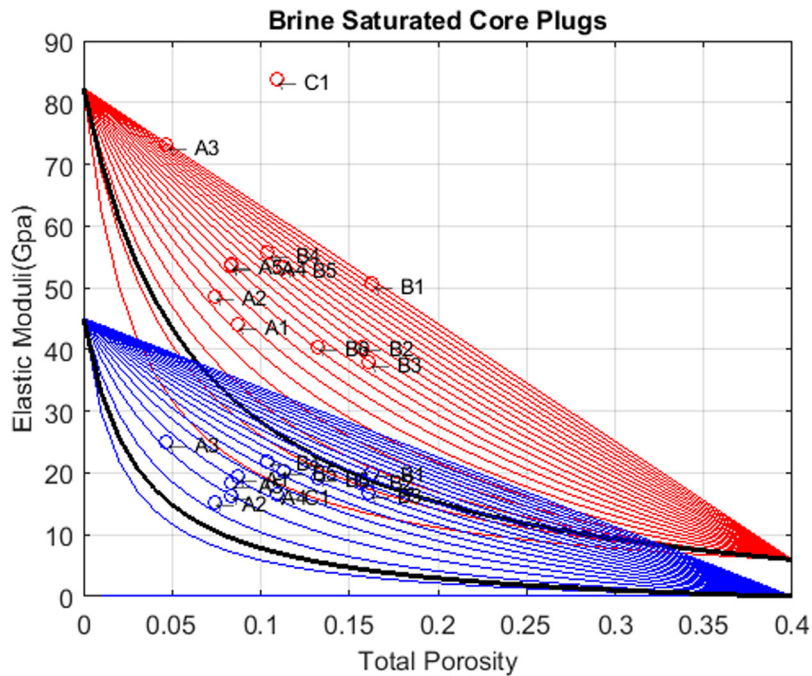


Figure 7. Bulk and shear moduli versus Archimedes porosity. The red curves (bulk moduli) and blue curves (shear moduli) are for $L = 0$ to $L = 1$ spanning all the data unless C1 sample is associated with an erroneous reading in P-wave travel time. No trend exists because there is a dual pore system of micro-pores and vugs. The black curves are the optimum microporosity fits the data. Red and blue circles are core plug measurements.

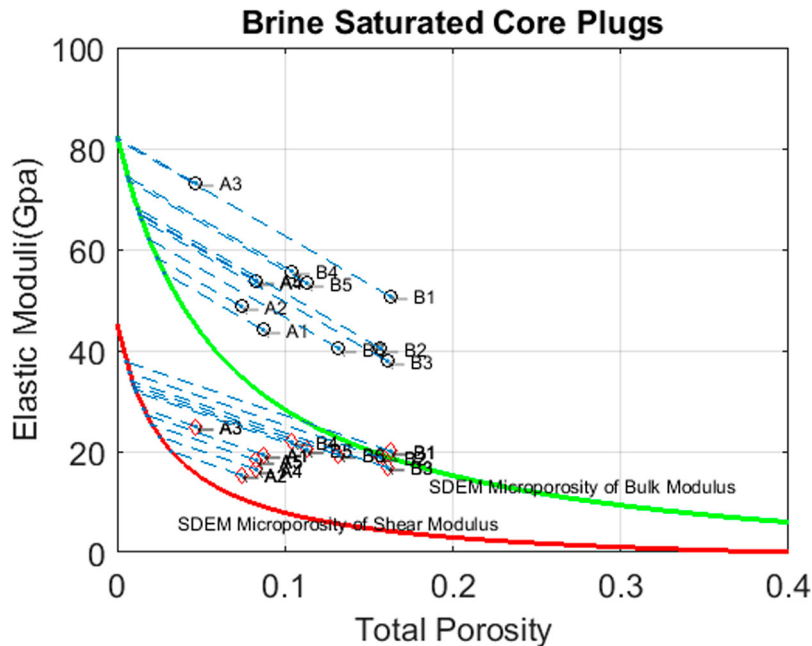


Figure 8. Bulk modulus and shear modulus versus Archimedes porosity. The optimum microporosity L parameters (red for shear and green for bulk modulus) are obtained from non-linear optimisation. The dashed blue lines are drawn using the $L = 1$ for vugs. Circles and rhombus are core plug measurements.

Multi-physics rock templates of carbonates in well log scale

On core scale measurements of resistivity and velocities, we found PCM and SDEM satisfactory to model pore structure of dual-porosity carbonates. Now, we will extend this methodology to well log scale.

Figure 10 illustrates a dual-porosity carbonate with 80 feet thickness which is partially saturated with oil

for the upper 37 ft. of the formation. The irreducible water saturation in the upper portion is about 0.1. The lower 33 ft. is water saturated and residual oil saturation is about 0.07 in this zone. The middle (~ 10 ft.) is the transition zone. Note that we assume two different pore networks are fully connected and that is why intergranular water saturation and vuggy water saturation are equal to total water saturation.

Table 2. SDEM model parameters. Note that vuggy porosity L parameters for bulk and shear moduli are set to 1.0 based on the previously published results (Myers and Hathon 2012). The rest of parameters are obtained from VFSA optimisation.

SDEM model parameters	Mean value
Critical porosity	0.40
Bulk modulus (GPa)	82.35
Shear modulus (GPa)	45.08
L parameter for microporosity & related to bulk modulus	0.07
L parameter for microporosity & related to shear modulus	0.07
L parameter for vuggy porosity & related to bulk modulus	1.00
L parameter for vuggy porosity & related to shear modulus	1.00
Lithology exponent for microporosity & related to resistivity	1.49
Lithology exponent for vuggy porosity & related to resistivity	1.06

Figure 11 displays the simulated well log responses over the dual-porosity carbonate formation shown in Figure 10. Bulk density (ρ_b) is modelled using mass conservation, P-wave slowness (DTCO) & S-wave slowness (DTSM) modelled using SDEM, and electrical resistivity (R_t) using PCM. Model parameters are summarised in Table 3. As expected, distinct fluid zones are separated on resistivity log in logarithmic scale and one can determine oil column, transition zone and water leg from reservoir top to bottom, respectively.

Figure 12 shows the variations of P&S-wave travel times (slowness) and velocities versus intergranular, vuggy, and total porosities. When plotting slowness/velocities versus total porosity, one can hardly trace any trend in the cloud of data. The same observations are seen for the case of plotting slowness/velocities with respect to vuggy porosity. In contrast, monotonic trends are easily observed when plotting slowness/velocities versus intergranular porosity. This is consistent

with the fact that secondary porosities are prone to be underestimated or overlooked by acoustic measurements (Kazatchenko, Markov, and Mousatov 2003).

Figure 13 illustrates traditional rock physics templates (Avseth, Mukerji, and Mavko 2005) created using velocity ratio (P-wave velocity divided to S-wave velocity) on the vertical axis and acoustic impedance (density times P-wave velocity) on the horizontal axis. Each panel is colour-coded with different petrophysical attributes including water saturation, total porosity, intergranular porosity and vuggy porosity. Starting with the panel colour-coded with water saturation, one can seamlessly see the separation of water-bearing from oil-bearing zones. Similar to the observations of Figure 12, the impact of intergranular porosity on velocity ratio and acoustic impedance is monotonic. In other words, by increasing intergranular porosity, velocity ratio increases and acoustic impedance decreases. On the contrary, no trends are seen between vuggy and total porosities and seismic attributes, i.e. velocity ratio and acoustic impedance. Consistent with the observations in Figure 12, secondary porosity is prone to be underestimated or overlooked by acoustic measurements (Kazatchenko, Markov, and Mousatov 2003).

Figure 14 shows the multiphysics rock templates highlighting the impact of intergranular porosity, vuggy porosity and water saturation on resistivity, P-wave slowness and S-wave slowness. Starting with the panel colour-coded with water saturation, one can seamlessly see the separation of water-bearing from oil-bearing zones. Similar to the observations of Figures 12 and 13,

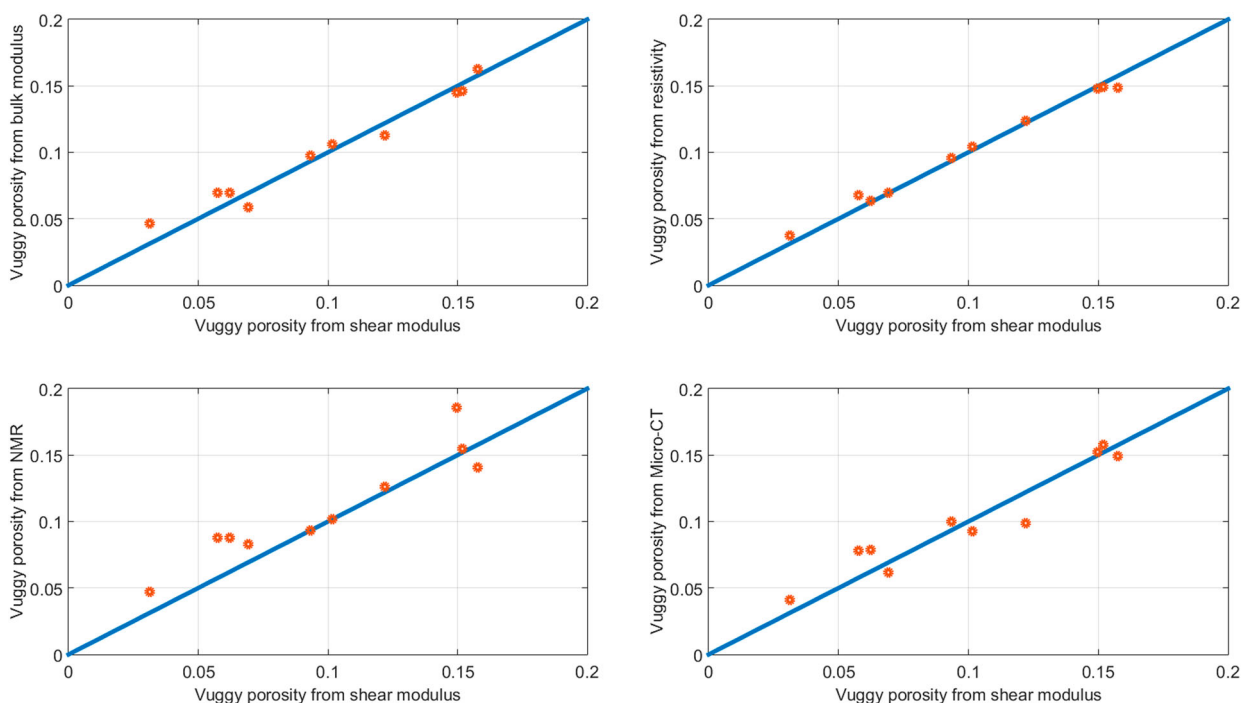


Figure 9. Comparison of vuggy porosities estimated from different methods. The bottom panels (lower left and lower right) indicate high correlations between velocity-derived vuggy porosity (shear modulus here) and vuggy porosity from independent measurements of NMR and micro-CT.

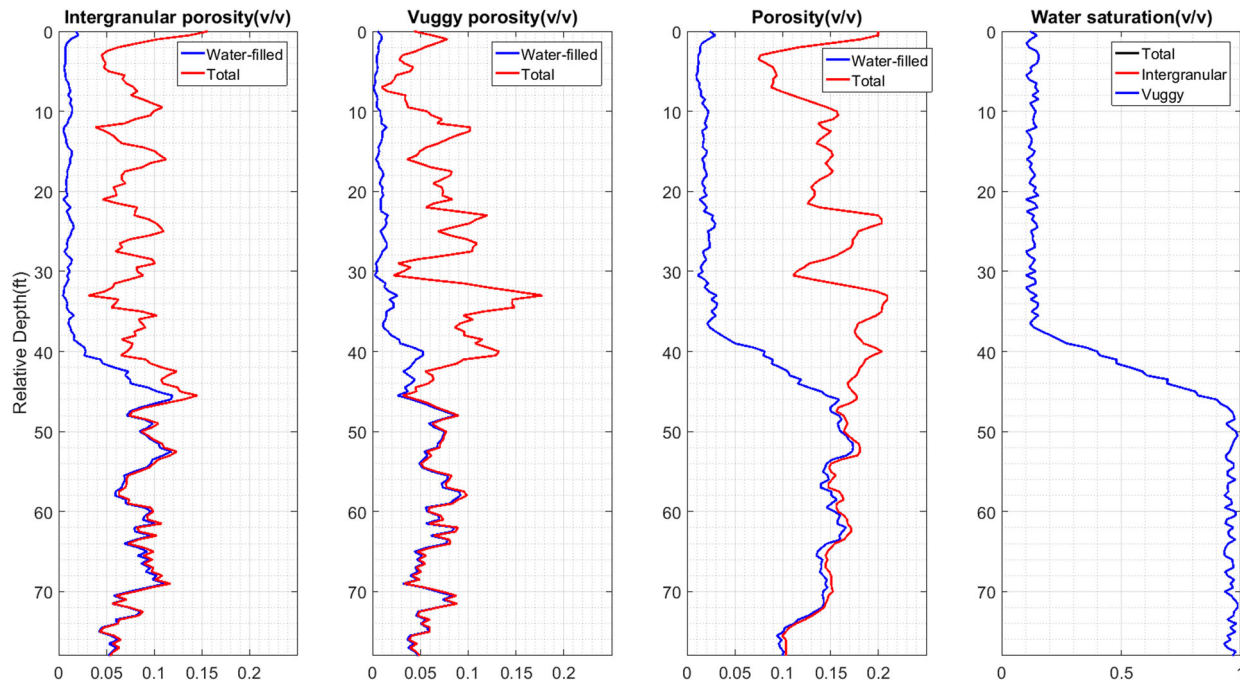


Figure 10. Plots of the true petrophysical properties over a dual-porosity carbonate formation containing intergranular and vuggy pores. In the first three tracks from left, red curves are intergranular, vuggy, and total porosities, respectively. For the same tracks, blue curves are water-filled porosities. The first track from the right shows intergranular water saturation, vuggy water saturation, and total water saturation which are equal at each depth interval.

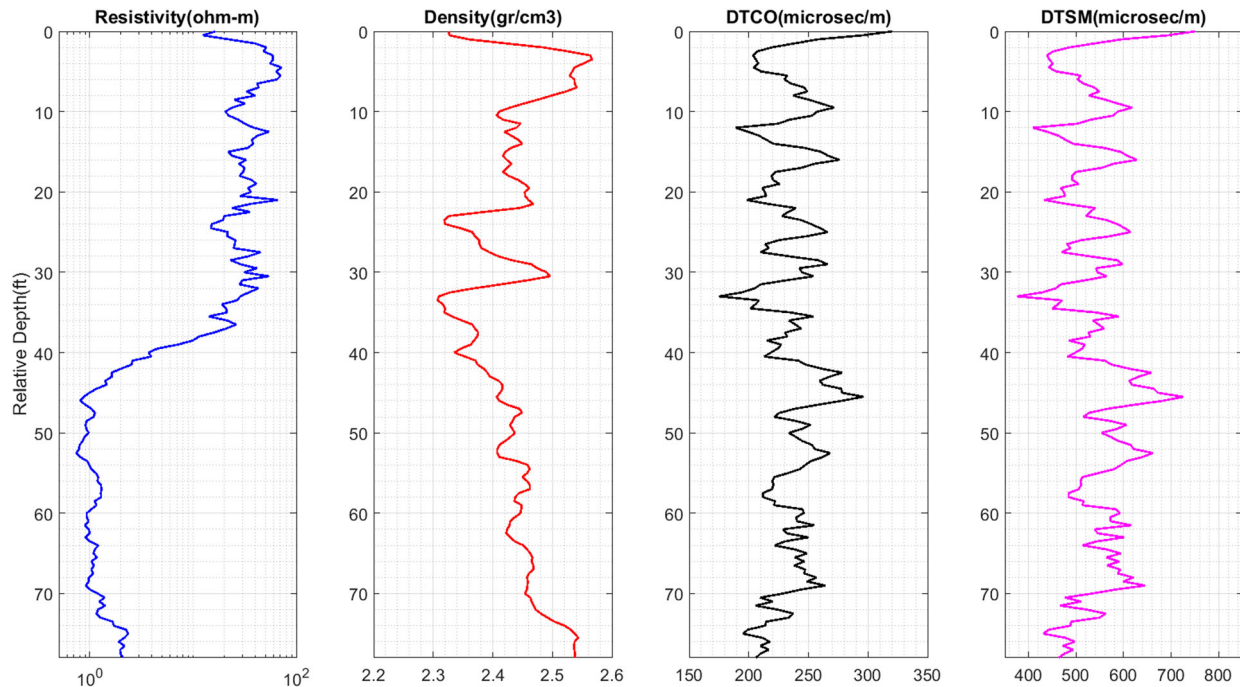


Figure 11. Plots of the well log responses simulated with proposed multi-physics modelling over the dual-porosity carbonate formation are illustrated in Figure 10. From left to right, the first track is electrical resistivity replicated with PCM, the second track is bulk density expressed by mass conservation, and the third and fourth tracks are compressional (P-wave) and shear (S-wave) slowness simulated with SDEM.

the impact of intergranular porosity is monotonic, but vuggy porosity has no clear trend in these crossplots.

To summarise all the observations, we depict the best RPT and MPRT in Figure 15 where the cross-plots of resistivity and elastic properties (slowness, velocity, acoustic impedance and velocity ratio) are displayed. The MPRT of this kind help interpreters to identify and

separate litho-fluid facies. We intentionally utilise two different rock templates in this figure. The first one is traditional RPT (Avseth, Mukerji, and Mavko 2005). These types of templates help seismic analysts to interpret seismic inversion results. The second kind of template is mainly derived from petrophysical properties including resistivity and compressional slowness (DTCO). These

Table 3. Reservoir, matrix, fluid, and model parameters for the dual-porosity carbonate formation

Properties	Symbol	Values	Units
Reservoir thickness	h	80	feet
Reservoir temperature	T	60	°C
Irreducible water saturation	S_{wirr}	0.1	Fractional
Residual oil saturation	S_{or}	0.07	Fractional
Salinity	Sal	120	Kppm
Matrix density	ρ_{ma}	2.71	g/cm³
Brine density	ρ_w	1.05	g/cm³
Oil density	ρ_o	0.75	g/cm³
Matrix bulk modulus	K_{ma}	77	GPa
Matrix shear modulus	μ_{ma}	32	GPa
Brine bulk modulus	K_w	2.5	GPa
Oil bulk modulus	K_o	0.75	GPa
Critical porosity	\emptyset_c	0.45	Fractional
Vuggy lithology exponent	λ_v	1.0	Fractional
Intergranular lithology exponent	λ_i	1.6	Fractional
Vuggy length scale for bulk modulus	L_v^k	1.0	Fractional
Intergranular length scale for bulk modulus	L_i^k	0.1	Fractional
Vuggy length scale for shear modulus	L_v^μ	1.0	Fractional
Intergranular length scale for shear modulus	L_i^μ	0.08	Fractional

types of templates help petrophysicists to interpret well logs.

In this paper, an objective function is defined as the root mean square of differences between simulated and observed well logs including density, resistivity, and P&S-wave slowness logs (DTCO and DTSM). Two sets of parameters are defined in the optimisation workflow.

Global parameters consist of matrix density, matrix bulk and shear moduli, salinity, critical porosity, intergranular lithology exponent for resistivity, intergranular L parameter (length scales) for bulk and shear moduli. Global parameters remain constant over the depth

interval of interest. Vuggy's lithology exponent for resistivity as well as vuggy's L parameters for bulk and shear moduli are set to 1.0 based on the previously published results (Myers and Hathon 2012). In VFSA optimisation structure, we evaluate the global error function to update the global model parameters.

Local model parameters changing as functions of depth include intergranular porosity (φ_i), vuggy porosity (φ_v), total porosity (φ_t) and water saturation (S_w) at each depth interval. In VFSA structure, we evaluate the local error function to update the local model parameters in the corresponding depth interval.

We design an objective function that has three terms. The first term is the difference between resistivity well log data ($R^{obs.}$) and modelled resistivity ($R^{sim.}$) using the PCM methodology. The second and third terms are the difference between DTCO and DTSM well log measurements ($DTCO^{obs.}$ and $DTSM^{obs.}$) and their corresponding simulated logs using the SDEM model ($DTCO^{Sim.}$ and $DTSM^{Sim.}$). Note that all the terms are normalised to the summation of well log observations and simulated well log responses. This will facilitate the quality control of error (objective or cost) function.

$$\Delta E = \frac{\sum_{i=1}^n (R^{sim.} - R^{obs.})^2}{\sum_{i=1}^n (R^{sim.} + R^{obs.})^2} + \frac{\sum_{i=1}^n (DTCO^{sim.} - DTCO^{obs.})^2}{\sum_{i=1}^n (DTCO^{sim.} + DTCO^{obs.})^2} + \frac{\sum_{i=1}^n (DTSM^{sim.} - DTSM^{obs.})^2}{\sum_{i=1}^n (DTSM^{sim.} + DTSM^{obs.})^2} \quad (10)$$

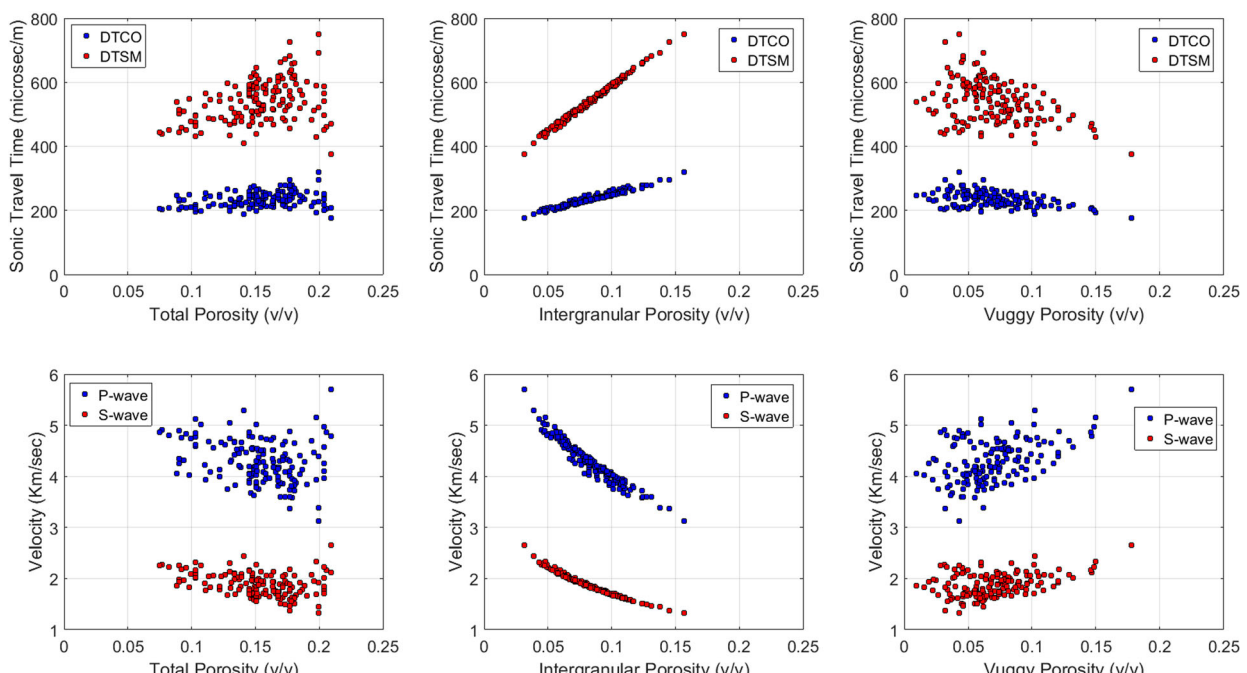


Figure 12. The variations of sonic travel times or slowness (top panels) and velocities (bottom panels) versus intergranular, vuggy, and total porosities. The blue dots are associated with S-wave (DTSM) and red dots corresponding to P-wave (DTCO) slowness/velocity.

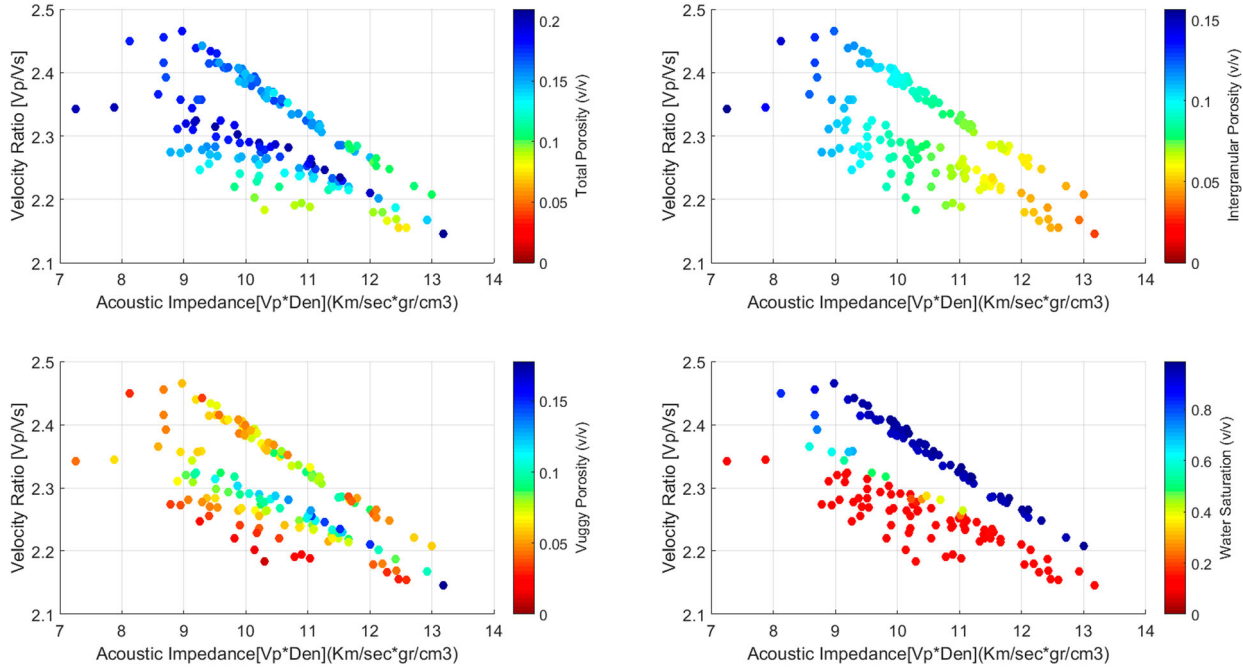


Figure 13. Traditional rock physics templates were created using velocity ratio (P-wave velocity divided to S-wave velocity) on the vertical axis and acoustic impedance (density times P-wave velocity) on the horizontal axis. Each panel is colour-coded with different petrophysical attributes highlighting the separation of water-bearing from oil-bearing zones and the impact of intergranular and vuggy porosities on velocity ratio and acoustic impedance (most common seismic attributes).

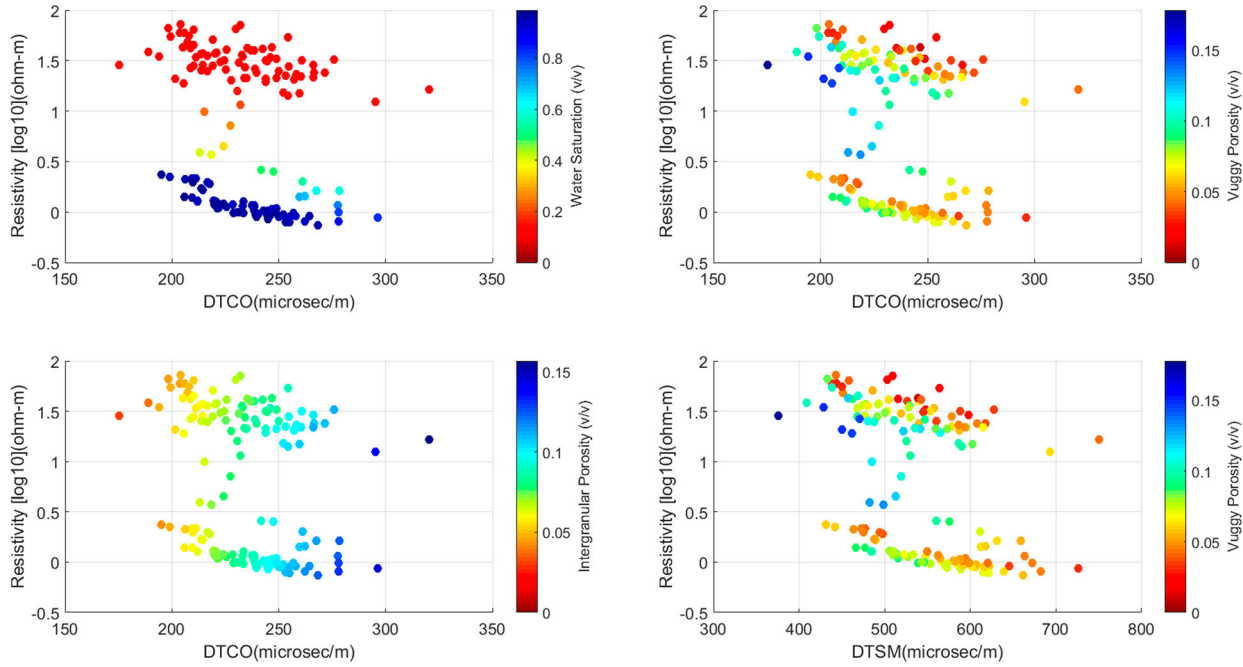


Figure 14. Multiphysics rock templates were created using different attributes highlighting the separation of water-bearing from oil-bearing zones and the impact of intergranular porosity on resistivity, P-wave slowness, and S-wave slowness. Right panels are color-coded with vuggy porosity. Top left panel is colour-coded with water saturation and bottom left panel is colour-coded with intergranular porosity.

We utilise the VFSA to minimise the objective function. To converge the VFSA optimisation and to obtain meaningful physical model parameters, we apply several constraints. Some of the important ones are as follows:

1. In each depth interval, the vuggy and intergranular porosities are smaller or equal to given total porosities.

$$\varphi_i \leq \varphi_t \quad (11)$$

$$\varphi_v \leq \varphi_t \quad (12)$$

2. In each depth interval, the sum of vuggy porosity and intergranular porosity should be equal to total

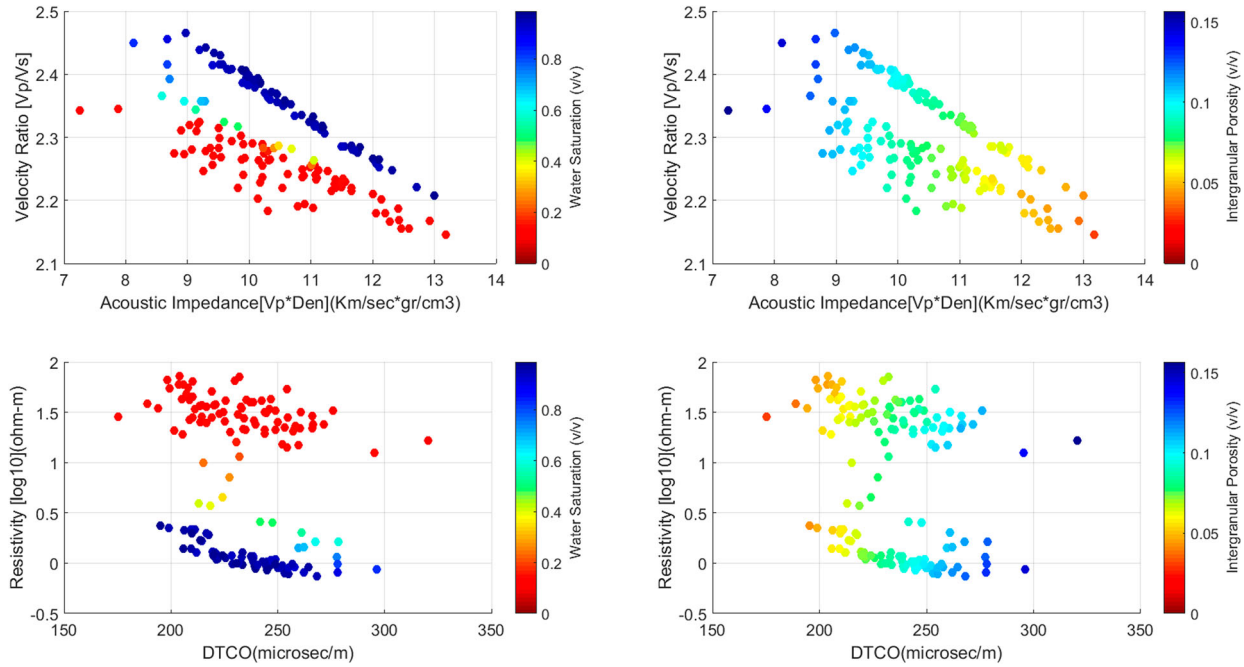


Figure 15. Multiphysics rock templates were created using different attributes. Left panels are colour-coded with water saturation and highlight the separation of water-bearing from oil-bearing zones. Right panels are colour-coded with intergranular porosity and highlight the impact of intergranular porosity on resistivity, velocity ratio, acoustic impedance and P-wave slowness.

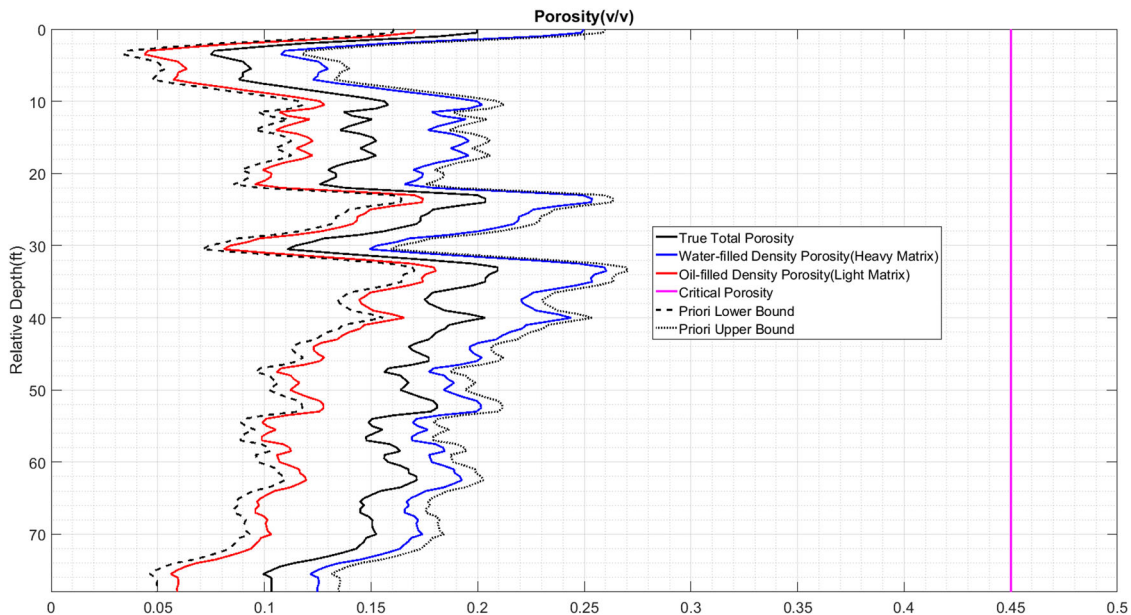


Figure 16. Plot of true total porosity, true critical porosity, density porosities obtained from density log assuming known matrices and fluids, and lower and upper bounds on total porosity to be used in VFSA optimisation.

porosities.

$$\varphi_i + \varphi_v = \varphi_t \quad (13)$$

3. The upper and lower search bounds on total porosity are computed from density log. Initial upper and lower bounds are first computed using a heavy mixture (heavy grain and water) and a light mixture (light grain and hydrocarbon), respectively. Then, safety factors in percentage are added to and subtracted from initial upper and lower bounds,

respectively, to form conservative search bounds (Figure 16).

In Figure 17, single realisation of true and inverted petrophysical properties and associated well log responses are overlaid in different panels. The inversion workflow is capable of matching the data for the three portions of carbonate formation (oil column, water leg and transition zone) and retrieving intergranular, vuggy, total and water-filled porosities with high precision.

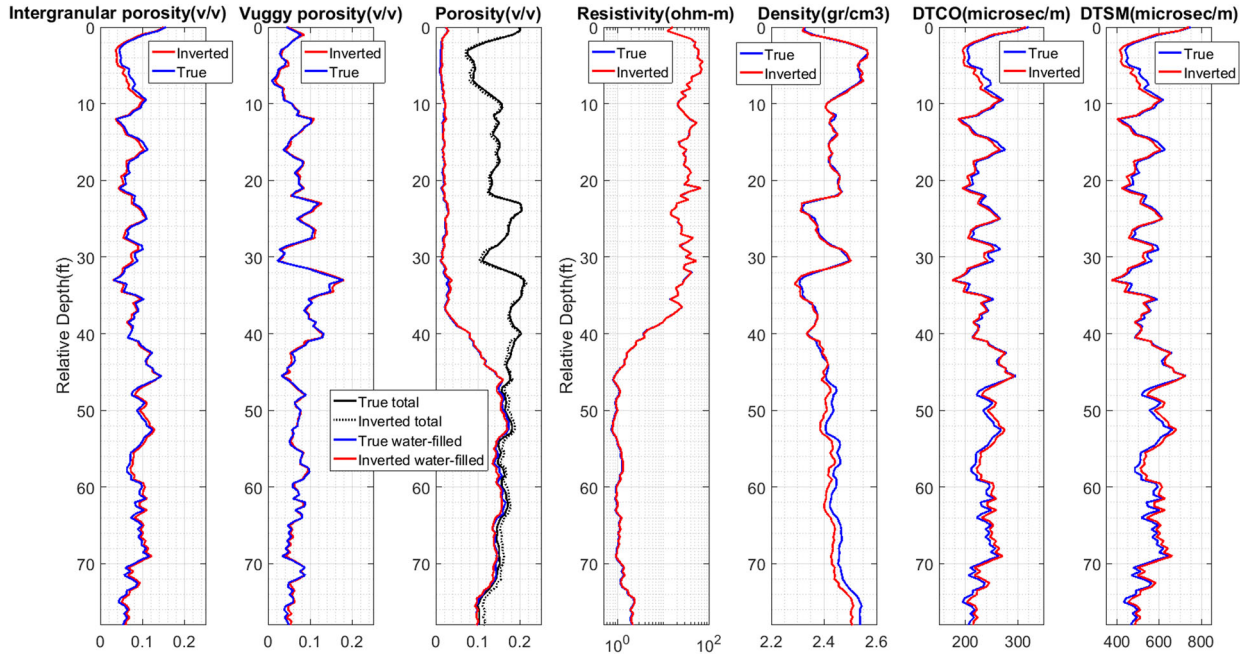


Figure 17. Plots of the true petrophysical properties, associated well log responses, and their inverted values for one single realisation. Dark blue curves display the true petrophysical properties and the associated well log responses, red curves show the inverted petrophysical properties and the inverted log responses. In the third track from left, true total porosity is shown in continuous black, the inverted total porosity in dotted black, true water-filled porosity in blue and inverted water-filled porosity in red.

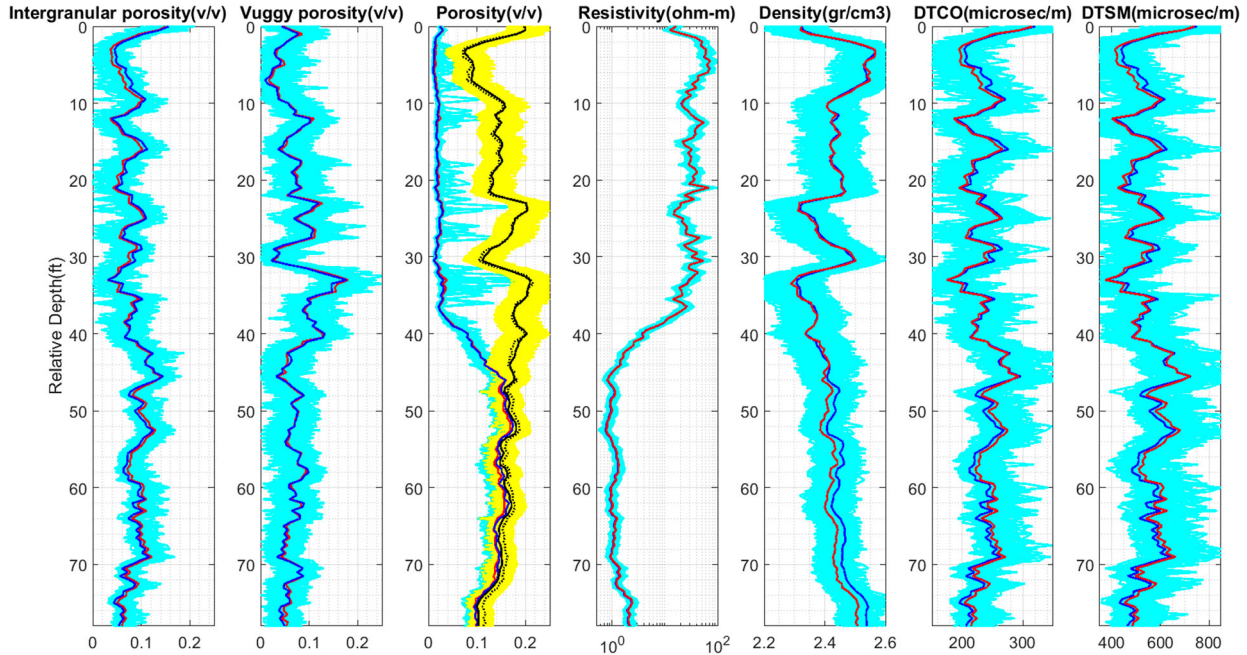


Figure 18. Plots of the true petrophysical properties, associated well log responses, and their inverted values for 100 realisations. Dark blue curves display the true petrophysical properties and the associated well log responses, red curves show the inverted petrophysical properties and the inverted log responses. The uncertainty in all parameters is shown by 100 realisations in cyan colour. Red curves are the mean values of all realisations. In the third track from left, true total porosity is shown in continuous black, the mean inverted total porosity in dotted black, true water-filled porosity in blue and mean inverted water-filled porosity in red (similar labelling as Figure 17). In this particular panel, the 100 realisations of total porosity are shown in yellow.

In Figure 18, true and inverted petrophysical properties and associated well log responses are overlaid in all panels for 100 realisations. Note that the mean of 100 independent realisations is very close to true petrophysical properties and associated well log responses. The inversion workflow is capable of matching the data for

the three portions of carbonate formation (oil column, water leg and transition zone) and retrieving intergranular, vuggy, total and water-filled porosities with high precision.

Figure 19 shows the performance of inversion workflow to recover global parameters by minimising the

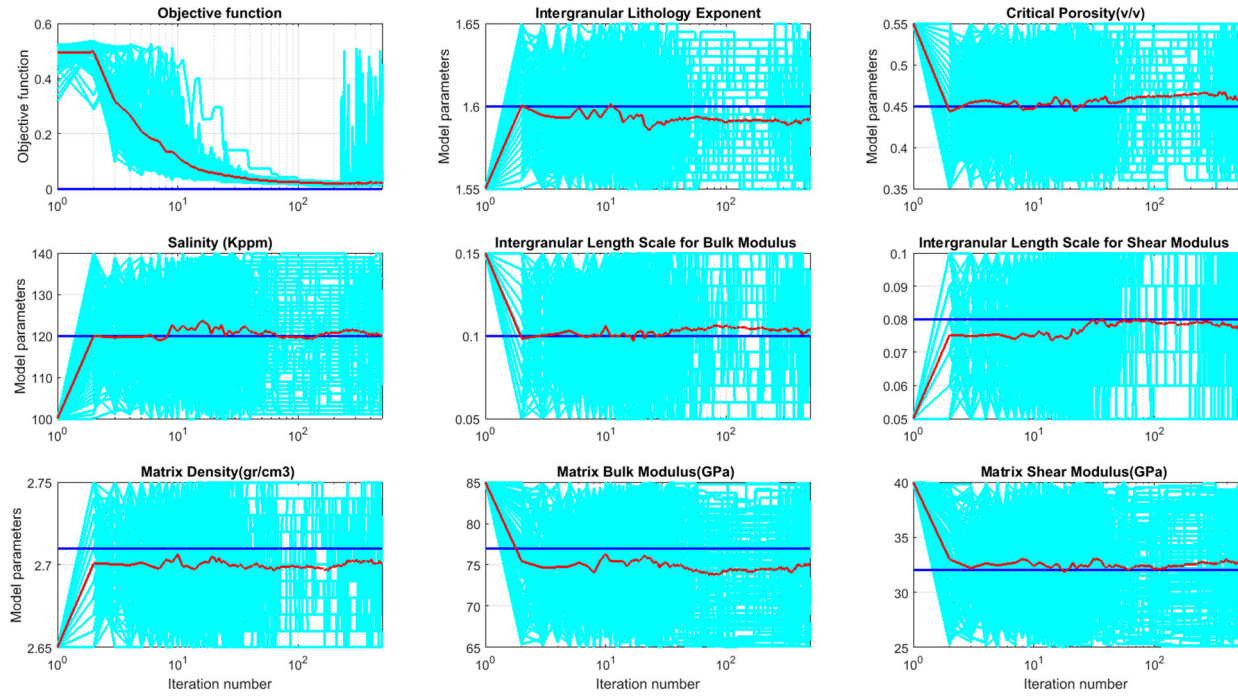


Figure 19. Evolution of normalised objective (error or cost) function, matrix and fluid properties, and PCM-SDEM model parameters. In all panels, blue curves are true or expected values, red curves are inverted parameters obtained from the averaging of 100 independent realisations shown in cyan colour.

normalised objective function. Note that the mean value of 100 realisations is close to the true value of each global parameter.

Discussion

To develop MPRT on core scale, we make three independent porosity measurements on carbonate core plugs including Archimedes, μ CT and NMR. We have modelled two pore types, microporosity and vuggy porosity. Resistivity, P& S-wave ultrasonic measurement of the same brine saturated core plugs was made. The joint modelling of resistivity and velocities was performed using the SDEM technique. The modelled vuggy versus matrix porosity is compared to the independently estimated porosities from NMR and μ CT. The parameters in the resistivity and velocity models are optimised in a global stochastic optimisation algorithm. The outcome of this stage will be the main core of subsequence well log and seismic data analyses.

To develop MPRT on well log scale, we observe that simulated well log responses match very well with true well logs (Figures 17 and 18). We also find that resistivity is the best resolved well log response. Sonic slowness logs (DTCO and DTSM) are reasonably recovered but not as good as resistivity. Density is well recovered in the oil column and transition zone, but inverted density has a negative shift from true density in the water leg. The same shifts, but positive and milder, are also observed in DTCO and DTSM logs leading to underestimate water-filled porosity in the water leg (Figure 17). Total porosity is the best-resolved parameter. Intergranular porosity

and vuggy porosity are the next resolved parameters. Water saturation is reasonably recovered, but not as good as other properties especially in the water leg as explained above. Salinity is the best resolved global parameter. Other global parameters are well recovered but not as good as salinity especially matrix properties (Figure 19).

Applying the proposed inversion algorithm on real well logs will shed light on any complexities (upscaling, invasion, tools' radius of investigation and vertical resolution, and reservoir thickness) not seen on our synthetic tests. This will be addressed in our future work when we will get access to real data from oil companies.

Conclusion

To develop MPRT on the core scale, we propose an integrated technique to jointly model the resistivity and velocities measurements using SDEM for dual-porosity carbonates. One of the salient features of this approach is its consistency in predicting vuggy and matrix porosities from different data sources. The optimisation algorithm has been able to fine-tune the model parameters of resistivity and velocity and provides vuggy and matrix porosities close to NMR and μ CT estimated porosities.

To develop MPRT on the well log scale, we construct the well log responses using the multiphysics models. We then design a customised VFSA search engine to perform a novel inversion workflow. Matrix properties (density and elastic moduli), salinity, critical porosity, PCM-SDEM model parameters, intergranular

porosity, vuggy porosity, total porosity and water saturation are the main properties estimated via this inversion algorithm.

The next logical step will be to extend this methodology by including other well logs (GR, Neutron, PEF, EPT and NMR). When fully developed, one can estimate the volumetric fraction of minerals, pore-type, porosity, saturation, matrix properties, salinity, critical porosity, resistivity lithology exponents and sonic length scales for different pore networks.

Disclosure statement

No potential conflict of interest was reported by the author(s).

References

- Archie, G.E. 1962. The electrical resistivity log as an aid in determining some reservoir characteristics. *Trans AIME* 146: 54–67.
- Avseth, P., T. Mukerji, and G. Mavko. 2005. *Quantitative seismic interpretation*. Cambridge University Press.
- Avseth, P., T. Mukerji, A. Jorstad, G. Mavko, and T. Veggeland. 2001. Seismic reservoir mapping from 3-D AVO in a North Sea turbidite system. *Geophysics* 66: 1157–1176.
- Gassmann, F. 1951. "Über die elastizität" at poroser medien. *Vierteljahrsschrift der Naturforschenden Gesellschaft* 96: 1–23.
- Ingber, L. 1989. Very fast simulated re-annealing. *Mathematical and Computer Modelling* Volume 12: 967–973.
- Ingber, L. 1993. Simulated annealing: practice versus theory. *Mathematical and Computer Modelling* Volume 18: 29–57.
- Kazatchenko, E., M. Markov, and A. Mousatov. 2003. Determination of primary and secondary porosity in carbonate formations using acoustic data, SPE 84209, The SPE Annual Technical Conference and Exhibition.
- Mavko, G., T. Mukerji, and J. Dvorkin. 2020. *The rock physics handbook*, (3rd Edition). Cambridge University Press.
- Myers, M.T. 1989. Pore combination modeling: extending the Hanai-Bruggeman equation: SPWLA 30th Annual Logging Symposium, 1989-D.
- Myers, M.T. 1991. Pore combination modeling: A technique for modeling the permeability and resistivity of complex pore systems: SPE Annual Technical Conference and Exhibition, 22662-MS.
- Myers, M.T., and L.A. Hathon. 2012. Staged differential effective medium (SDEM) models for the acoustic velocity in carbonates. *American Rock Mechanic Association* 12: 553.
- Mukerji, T., P. Avseth, G. Mavko, I. Takahashi, and E.F. González. 2001. Statistical rock physics: combining rock physics, information theory, and geostatistics to reduce uncertainty in seismic reservoir characterization. *The Leading Edge* 20 no. 3: 313.
- Nur, A., G. Mavko, J. Dvorkin, and D. Gal. 1995. Critical porosity: the key to relating physical properties to porosity in rocks, Proc. 65th Ann. Int. Meeting, Society of Exploration Geophysicists, 878.
- Rovetta, D., D. Colombo, and E. Turkoglu. 2017. Petrophysical joint inversion of multi-geophysical attributes and measurements for reservoir characterization, SPE-184030-MS.
- Salma, S., E. Turkoglu, and D. Rovetta. 2018. Application of petrophysical joint inversion to a carbonate reservoir in Saudi Arabia. *SEG Technical Program Expanded Abstracts*, 3342–3346.
- Shahin, A., M.T. Myers, and L.A. Hathon. 2020. Global optimization to retrieve borehole-derived petrophysical properties of carbonates. *Geophysics* 85 no. 3: D75–D82.